Atomic ordering in the doped rare earth cobaltates $Ln_{0.33}Sr_{0.67}CoO_{3-\delta}$ ($Ln = Y^{3+}$, Ho^{3+} and Dy^{3+})

R.L. Withers,[a,*] M. James,[b] and D.J. Goossens[b]

[a] Research School of Chemistry, Australian National University, GPO Box 4, Canberra ACT 0200, Australia
[b] Neutron Scattering Group, Australian Nuclear Science and Technology Organisation, PMB 1, Menai NSW 2234, Australia

Abstract

The perovskite-based rare earth cobaltates ($Ln_{0.33}Sr_{0.67}CoO_{3-\delta}$) ($Ln = Y^{3+}$, Ho^{3+} and Dy^{3+}) have been synthesized at 1100°C under 1 atm oxygen. A thermogravimetric study has determined the overall oxygen content in each case while a combined electron diffraction (ED) and synchrotron X-ray diffraction study has revealed the presence of a complex, previously unreported, perovskite-related superstructure phase. ED gave a resultant $C1c1$ but most probably $Cmcm$ ($\mathbf{a} = 2a_p - 2c_p$, $\mathbf{b} = 4b_p$, $\mathbf{c} = 2a_p + 2c_p$) perovskite-related superstructure, describable as a modulated $I4/mmm$ intermediate parent structure. Synchrotron X-ray data has been used to refine the intermediate parent structures of all three compounds. Coupled Ln/Sr and O/vacancy ordering and associated structural relaxation is shown to be responsible for the observed superstructure.
© 2003 Elsevier Science (USA). All rights reserved.

1. Introduction

Perovskite-based rare earth cobaltates ($Ln_{1-x}Sr_xCoO_{3-\delta}$) ($Ln$ = lanthanide ion) have attracted significant attention over recent years due to potential applications in solid oxide fuel cells [1–4] and as ceramic membranes for high temperature oxygen separation [5,6]. The materials also show a wide range of interesting magnetic responses including glassy behavior [7–9] and room temperature ferromagnetism [10–15]. While the structure and physical properties of the Ln = La end-member, $La_{1-x}Sr_xCoO_{3-\delta}$, have been extensively studied [16–21], it is only more recently that researchers have begun to take substantial interest in perovskite-related phases of this type containing the smaller lanthanide ions [22–26].

The attractive physical properties of these materials are strongly dependent upon overall oxygen content as well as local, or longer range, ordering (Ln^{3+}/Sr^{2+}, O/vacancy and Co^{3+}/Co^{4+}). Oxygen ionic conductivity, for example, is known to be strongly affected by oxygen vacancy ordering and associated structural relaxation [3] while magnetic behavior will clearly be strongly affected by the related Co^{3+}/Co^{4+} ratio and distribution. To date, however, there has been remarkably little investigation of the structure and local crystal chemistry of these perovskite-related materials.

Long range ordering and associated structural relaxation typically give rise to superstructure phases characterized by the existence of weak additional satellite reflections in addition to the strong Bragg reflections of an underlying perovskite-type average structure [27,28]. The detection and characterization of such superstructure phases is often difficult from powder X-ray diffraction (XRD) alone both because of the low intensity of satellite reflections and the fact that the metric symmetry of the resultant superstructure phases typically remains very close to cubic, giving rise to a strong tendency for (often) fine scale twinning and difficulties in space group assignment and refinement [27–32]. The structural characterization of such perovskite-related superstructure phases calls for a multi-technique investigation.

In this paper, we present the results of a combined thermogravimetric, electron diffraction (ED) and synchrotron XRD analysis of a recently discovered, new

*Corresponding author. Fax: +61-26-125-0750.
E-mail address: withers@rsc.anu.edu.au (R.L. Withers).

superstructure phase in the $Ln_{0.33}Sr_{0.67}CoO_{3-\delta}$, ($Ln = Y^{3+}$, Ho^{3+} and Dy^{3+}) systems.

2. Experimental

2.1. Synthesis

Polycrystalline samples of $Ln_{0.33}Sr_{0.67}CoO_{3-\delta}$ were prepared from spectroscopic grade powders of $SrCO_3$ (98 + %), $Co(NO_3)_2 \cdot 6H_2O$ (98%) and either Y_2O_3 (99.99%), Dy_2O_3 (99.9%) or $Ho(NO_3)_3 \cdot 5H_2O$ (99.9%). The powders were dissolved in dilute nitric acid and an intimate mixture of the metal oxides was formed via the decomposition of a citric acid–ethylene glycol sol–gel. The residues were pelleted and sintered in a tube furnace at 1100°C under flowing oxygen for up to 3 days with intermediate re-grinding and re-pelleting until no further reaction was evident by powder X-ray diffraction.

2.2. Thermogravimetry

Thermogravimetry of ca. 70 mg of each of the $Ln_{0.33}Sr_{0.67}CoO_{3-\delta}$ samples were carried out using a SETARAM TAG24 Simultaneous Thermogravimetric and Differential Thermal Analyser. The samples were reduced under a mixture of 3.5% hydrogen in nitrogen over a temperature range of 25–900°C at a heating rate of 5°C/min. Each of the samples studied decomposed under hydrogen reduction to give the component oxides Ln_2O_3 and SrO as well as Co metal. As has been shown for other rare earth perovskite cobaltates [33], the observed mass loss is therefore apportioned to the change in oxygen content as Co^{n+} in the as-synthesized sample is reduced to Co metal.

2.3. Electron diffraction

ED was carried out using a Philips EM 430 Transmission Electron Microscope operating at 300 kV. Samples suitable for TEM work were prepared by the dispersion of finely ground material onto a holey carbon film.

2.4. Powder diffraction measurements

Powder synchrotron diffraction data were collected at the Australian National Beamline Facility (ANBF), Tsukuba, Japan. Samples were mounted in 0.5 mm quartz capillaries and diffraction data collected in transmission mode using $\lambda = 0.99868$ Å synchrotron radiation and an image plate detector system [34]. Structure refinements were carried out by the Rietveld method [35] using the RIETICA program [36] with pseudo-Voigt peak shapes and refined backgrounds. Further details of the crystal structure investigations can be obtained from the Fachinformationszentrum Karlsruhe, 76344 Eggenstein-Leopoldshafen, Germany (fax: +49-7247-808-66; mailto: crysdata@fiz-karlsruhe.de) on quoting the depository number CSD-412937 for $Y_{0.33}Sr_{0.67}CoO_{2.79}$, CSD-412938 for $Dy_{0.33}Sr_{0.67}CoO_{2.78}$ and CSD-412939 for $Ho_{0.33}Sr_{0.67}CoO_{2.76}$.

3. Results

3.1. Thermogravimetry

The overall oxygen content and average cobalt oxidation state for samples 1–3 were determined based on the results of thermogravimetric analysis (Table 1). The oxygen contents (atoms per $Ln_{0.33}Sr_{0.67}CoO_{3-\delta}$ formula unit) range between 2.76 (for 3) and 2.79 (for 1), leading to average Co^{n+} oxidation states of 3.25, 3.23

Table 1
Crystallographic data for intermediate $I4/mmm$ parent structure of 1, 2 and 3 as determined from synchrotron X-ray diffraction data

	1	2	3
Formula[a]	$Y_{0.33}Sr_{0.67}CoO_{2.79}$	$Dy_{0.33}Sr_{0.67}CoO_{2.78}$	$Ho_{0.33}Sr_{0.67}CoO_{2.76}$
Formula weight	191.618	215.744	216.706
Co^{3+}; Co^{4+} (%)[a]	75; 25	77; 23	81; 19
Space group	$I4/mmm$ (No. 139)	$I4/mmm$ (No. 139)	$I4/mmm$ (No. 139)
Z	16	16	16
a (Å)	7.6282(2)	7.6129(1)	7.6188(1)
c (Å)	15.3337(4)	15.3450(2)	15.3079(2)
V (Å³)	892.27(3)	889.35(2)	888.57(1)
ρ_{calc} (g cm^{-3})	5.693	6.445	6.475
2θ range (deg)	5–84	5–84	5–84
λ (Å)	0.99868	0.99868	0.99868
No. of reflns	305	304	304
$R_P/R_{WP}/R_{Bragg}$	4.4%/6.6%/7.0%	2.5%/3.5%/8.1%	3.0%/4.1%/5.2%

[a] Oxygen content and ratio of cobalt oxidation states as determined by thermogravimetry.

and 3.19 for **1**, **2**, and **3**, respectively. Thus, it is expected that between 19% and 25% of the cobalt present in these phases is present as Co(IV), while the remaining cobalt is present as Co(III) (Table 1). While the level of oxygen vacancies present in these phases is quite high ($\sim 7.5-8.8$%), it is consistent with the behavior observed at similar Sr^{2+} doping levels in other perovskite-based rare earth cobaltates [22–24].

3.2. Powder synchrotron X-ray diffraction (XRD)

Fig. 1 shows the first of three histograms of synchrotron XRD data (over the 2θ range from $5°$ to $42°$) for $Y_{0.33}Sr_{0.67}CoO_{2.79}$ (**1**), $Dy_{0.33}Sr_{0.67}CoO_{2.78}$ (**2**) and $Ho_{0.33}Sr_{0.67}CoO_{2.76}$ (**3**), respectively. The parent perovskite-type reflections are shown labelled with a subscript p. (A blow-up of the region from $25°$ to $31°$ and including the unsplit $\langle 111 \rangle_p^*$ and the split $\langle 002 \rangle_p^*$ peaks has been included as an inset for each of a, b and c.) As expected, the strongest reflections (in particular $\langle 011 \rangle_p^*$ but also $\langle 111 \rangle_p^*$, $\langle 002 \rangle_p^*$, $\langle 112 \rangle_p^*$) belong to the underlying P-centered, perovskite parent sub-structure. While the $\langle 111 \rangle_p^*$ line is not split, the $\langle 001 \rangle_p^*$, $\langle 011 \rangle_p^*$, $\langle 002 \rangle_p^*$ and $\langle 112 \rangle_p^*$ lines have each separated into two distinct lines with an intensity ratio of $\sim 1:2$. (The extent of this splitting is most apparent for the $Ln = Dy$ compound but is also detectable for both the Ho and Y compounds.) In the case of the $\langle 002 \rangle_p^*$ and $\langle 112 \rangle_p^*$ lines, the weaker half of the doublet is always on the low angle side whilst, in the case of the $\langle 110 \rangle_p^*$ line, the reverse is the case. The metric symmetry of each compound is thus tetragonal rather than cubic with the unique cell dimension larger than the two remaining, symmetry-linked cell dimensions. Refinement of the underlying tetragonal parent sub-structure cell dimensions gave lattice parameters $a_p = c_p = 3.8141(1)$ Å, $b_p = 3.8334(2)$ Å for the Y compound, $a_p = c_p = 3.8065(1)$ Å, $b_p = 3.8363(1)$ Å for the Dy compound and $a_p = c_p = 3.8094(1)$ Å, $b_p = 3.8270(1)$ Å for the Ho compound.

In addition to these strong perovskite parent reflections (labelled **G** in what follows), there also exist numerous weak additional satellite reflections (particularly apparent in the case of the $Ln = Dy$ and Ho compounds at low 2θ). Note that 3 out of 4 of these satellite reflections visible at low angle ($2\theta < \sim 15°$) are clearly present for the $Ln = Dy$ and Ho compounds but disappear for the $Ln = Y$ compound when the compositional contrast between the Ln and Sr vanishes. (ED makes plain (see below) that this is not because the Y compound has a different superstructure to the Dy and Ho compounds.) Given that compositional ordering is known to be most apparent at low 2θ, it is clear that Ln/Sr ordering will be essential in order to fit to these observed satellite reflections. It was not, however, possible to unambiguously determine a unit cell and

space group symmetry from the XRD data until after the results of the ED study (see below).

3.3. Electron diffraction

Fig. 2a shows a commonly observed $\langle 100 \rangle_p$ type ED pattern (EDP) of the $Ln = Ho$ compound but representative of all three compounds. (The three compounds were found to be completely isomorphous from the ED point of view and equivalent zone axis EDPs to those shown below were found for all three compounds.) Notice the presence of relatively strong $\mathbf{G} \pm 1/2 \langle 010 \rangle_p^*$ and $\mathbf{G} \pm 1/4 \langle 012 \rangle_p^*$ type satellite reflections as well as a multitude of additional weaker satellite reflections of the form $\mathbf{G} \pm m(1/4) [010]_p^* \pm n(1/4) [001]_p^*$ (m, n integers). An observed rapid variation in the relative intensity of one class of these superlattice reflections relative to another upon small translations of the beam relative to the sample strongly suggested the presence of micro-twinning. The prevalence of, and difficulty in detecting, this twinning as well as the fact that not all of these additional satellite reflections simultaneously co-exist in any one local region is apparent from the equivalent single domain $[100]_p$ type EDP (obtained by careful positioning of the incident electron beam) shown in Fig. 2b. Indeed, in Fig. 2b, only the $\mathbf{G} \pm 1/2 [010]_p^*$ and $\mathbf{G} \pm 1/4 [012]_p^*$ type satellite reflections remain. Clearly, the four-fold axis around a_p as well as the tertiary $\langle 011 \rangle_p$ type mirrors present in the $Pm3m$ parent structure are broken in the superstructure. (The effect of the twinning apparent in Fig. 2a is, as expected, to apparently restore these broken symmetry elements cf. Fig. 2a with b.)

Fig. 3a shows a typical $\langle 101 \rangle_p$ type zone axis EDP obtained by tilting $45°$ away from Fig. 2a while keeping the $[010]_p^*$ systematic row excited. Note the strong presence of sharp, well-defined $\mathbf{G} \pm 1/2 [101]_p^*$ and $\mathbf{G} \pm 1/2 [010]_p^*$ satellite reflections in addition to the presence of a rather weaker and somewhat streaked (along $[010]_p^*$) class of satellite reflections of the form $\mathbf{G} \pm 1/4 \langle 101 \rangle_p^*$ and $\mathbf{G} \pm 1/4 \langle 111 \rangle_p^*$. Notice also the double density of reflections in the weak, streaked rows of satellite reflections relative to the alternate rows of Bragg reflections. Such an occurrence is quite commonly observed (indeed it is difficult to avoid). Fig. 4, for example, shows an EDP obtained by tilting 5–10° away from the exact $[100]_p$ zone axis orientation of Fig. 2b (keeping the $[001]_p^*$ systematic row excited) so as to bring up the various satellite higher order Laue zone (HOLZ) layer reflections. Note the doubled density of reflections in alternate HOLZ layers (one such HOLZ layer is arrowed in Fig. 4) and the presence of streaking (again along $[010]_p^*$) in these double density layers.

Such observations cannot be explained in conventional 3-d crystallographic terms and suggest the presence of a further, rather more fine scale, form of twinning. This is confirmed by the equivalent
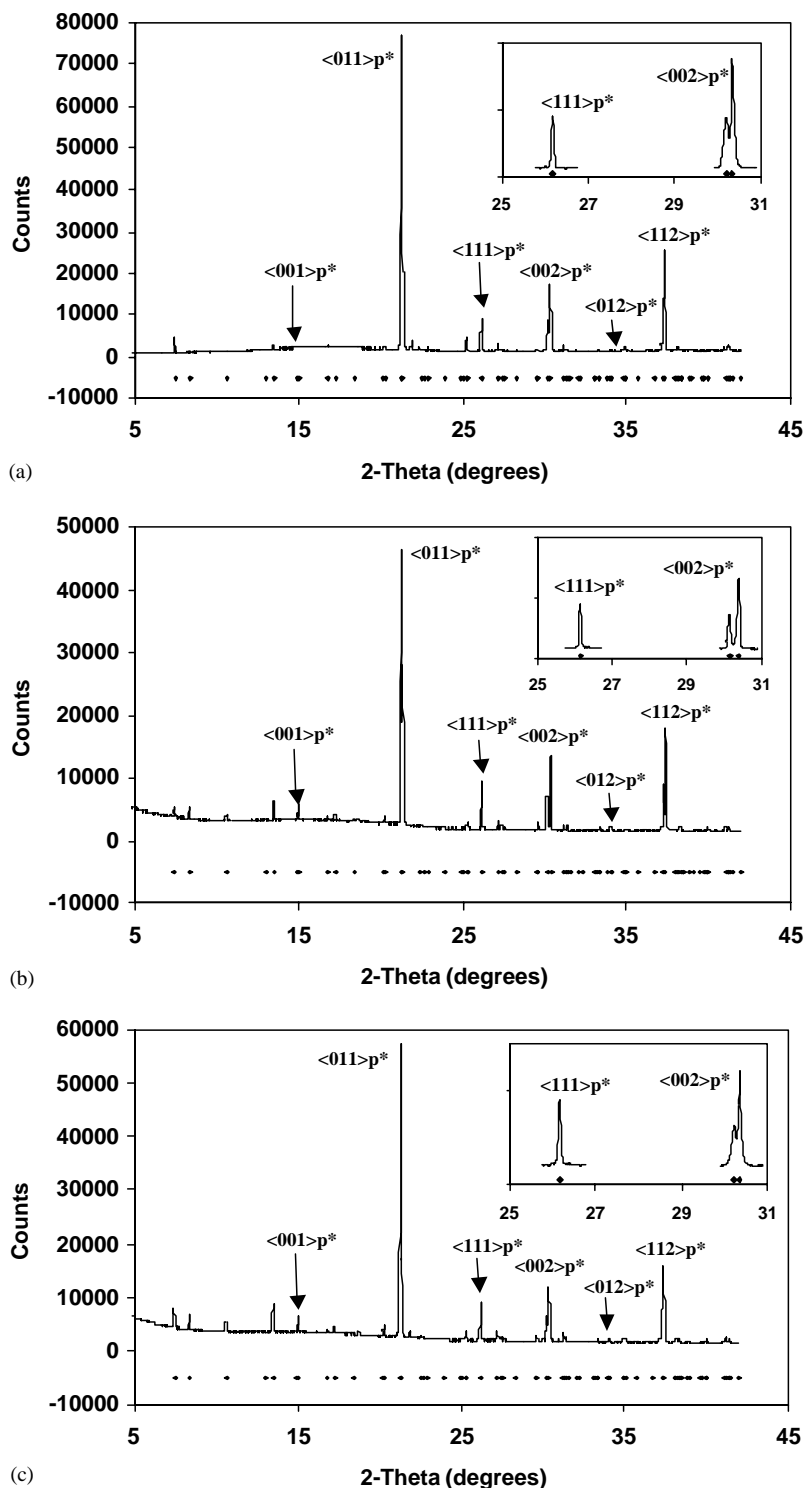
Fig. 1. The first histograms of synchrotron data for (a) $Y_{0.33}Sr_{0.67}CoO_{2.79}$ (**1**), (b) $Dy_{0.33}Sr_{0.67}CoO_{2.79}$ (**2**) and (c) $Ho_{0.33}Sr_{0.67}CoO_{2.79}$ (**3**). The parent perovskite-type reflections are shown labelled with a subscript p. The reflections markers underneath correspond to those of an F-centered $\mathbf{a} = 2a_p - 2c_p, \mathbf{b} = 4b_p, \mathbf{c} = 2a_p + 2c_p$ supercell (see the text for details). (A blow-up of the region from 25° to 31° and including the unsplit $\langle 111 \rangle_p^*$ and the split $\langle 002 \rangle_p^*$ peaks has been included as an inset for each of *a*, *b* and *c*).

(to Fig. 3a) non-twinned or single domain $[101]_p$ EDP shown in Fig. 3b. Here the $\mathbf{G} \pm 1/4 \langle 111 \rangle_p^*$ satellite reflections of Fig. 3a are present but not the $\mathbf{G} \pm 1/4 \langle 101 \rangle_p^*$ satellite reflections. This fine scale form of

twinning is much more difficult to detect even via electron micro-diffraction suggesting that it typically occurs on a fine scale $< \sim 20$ nm. The twin plane would appear to be $[010]_p$ giving rise to the commonly observed
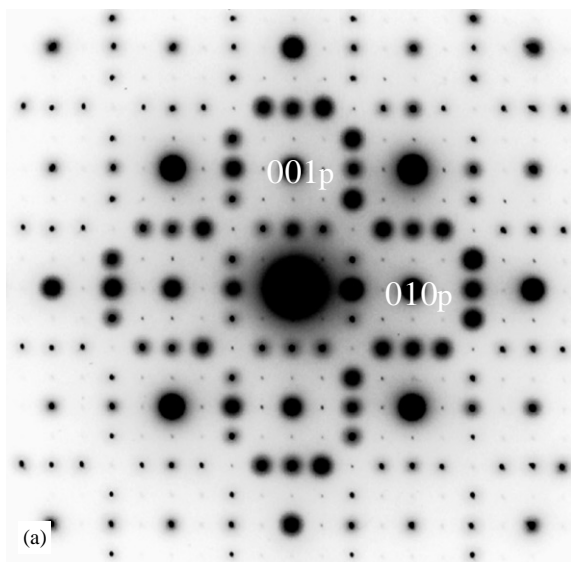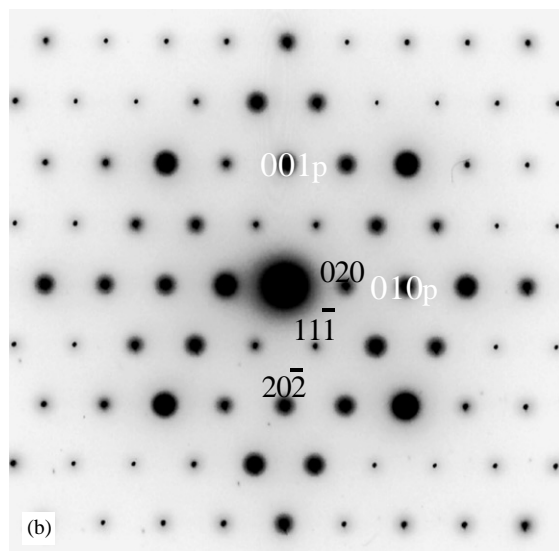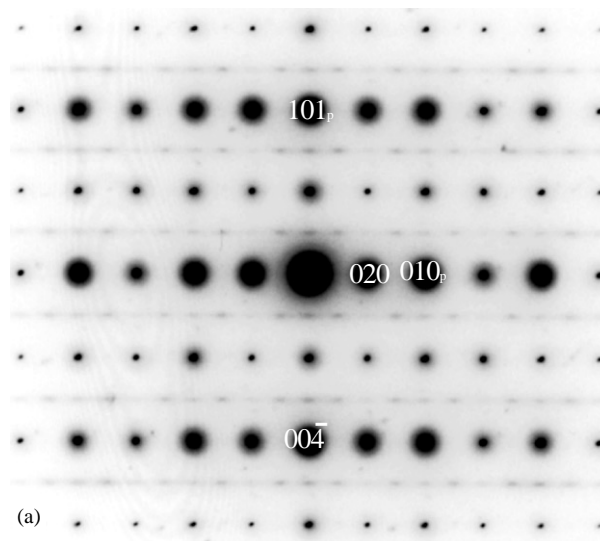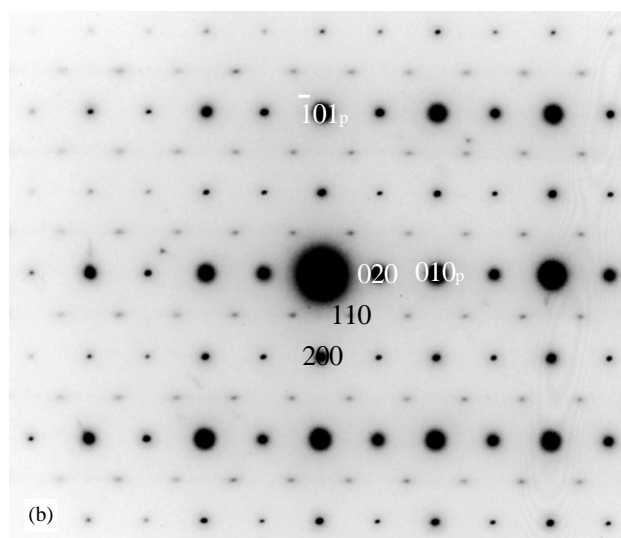
Fig. 2. (a) A commonly observed twinned $\langle 100 \rangle_p$ type EDP of the $Ln = Y$ compound but representative of all three compounds. Notice the presence of relatively strong $\mathbf{G} \pm 1/2 \langle 010 \rangle_p^*$ and $\mathbf{G} \pm 1/4 \langle 012 \rangle_p^*$ type satellite reflections as well as a multitude of additional weaker satellite reflections of the form $\mathbf{G} \pm m(1/4) [010]_p^* \pm n(1/4) [001]_p^*$ (m, n integers). (b) The equivalent single domain $[100]_p$ type EDP (obtained by careful positioning of the incident electron beam). The parent perovskite-type reflections are shown labelled with a subscript p. Indexation without the subscript p is with respect to an $\mathbf{a} = 2a_p - 2c_p$, $\mathbf{b} = 4b_p$, $\mathbf{c} = 2a_p + 2c_p$ ($\mathbf{a}^* = 1/4\ [10\bar{1}]_p^*$, $\mathbf{b}^* = 1/4\ [010]_p^*$, $\mathbf{c}^* = 1/4\ [101]_p^*$) supercell.

Fig. 3. (a) A typical $\langle 101 \rangle_p$ type zone axis EDP obtained by tilting $45°$ away from the $\langle 100 \rangle_p$ type EDP of Fig. 2a while keeping the $[010]_p^*$ systematic row excited. Note the strong presence of sharp, well-defined $\mathbf{G} \pm 1/2\ [101]_p^*$ and $\mathbf{G} \pm 1/2\ [010]_p^*$ satellite reflections in addition to the presence of a rather weaker and somewhat streaked (along $[010]_p^*$) class of satellite reflections of the form $\mathbf{G} \pm 1/4\ \langle 101 \rangle_p^*$ and $\mathbf{G} \pm 1/4\ \langle 111 \rangle_p^*$. (b) The equivalent non-twinned or single domain $[101]_p$ EDP. Here the $\mathbf{G} \pm 1/4\ \langle 111 \rangle_p^*$ satellite reflections of Fig. 3a are present but not the $\mathbf{G} \pm 1/4\ \langle 101 \rangle_p^*$ satellite reflections. The parent perovskite-type reflections are shown labelled with a subscript p. Indexation without the subscript p is with respect to an $\mathbf{a} = 2a_p - 2c_p$, $\mathbf{b} = 4b_p$, $\mathbf{c} = 2a_p + 2c_p$ ($\mathbf{a}^* = 1/4\ [10\bar{1}]_p^*$, $\mathbf{b}^* = 1/4\ [010]_p^*$, $\mathbf{c}^* = 1/4\ [101]_p^*$) supercell.

diffuse streaking of the class of weak satellite reflections along $[010]_p^*$.

The only reciprocal lattice unit cell consistent with all of the above ED evidence is given by $\mathbf{a}^* = 1/4\ [10\bar{1}]_p^*$, $\mathbf{b}^* = 1/4\ [010]_p^*$ and $\mathbf{c}^* = 1/4\ [101]_p^*$ when indexed with respect to the underlying perovskite parent structure. Indexation without the subscript p in Figs. 2b, 3 and 4 is with respect to this basis vector set. The corresponding

$(2\sqrt{2}a_p \times 4b_p \times 2\sqrt{2}c_p)$ C-centered real space unit cell is given by $\mathbf{a} = 2a_p - 2c_p$, $\mathbf{b} = 4b_p$, $\mathbf{c} = 2a_p + 2c_p$. No characteristic extinction condition other than the C-centered condition, $F(hkl) = 0$ unless $h + k$ is even, is observed in the single domain [101] (see Fig. 2b) or [001] (see Fig. 3b) zone axis EDPs. C-centering is also consistent with the $\langle 101 \rangle_p$ zone axis EDP shown in Fig. 3a provided this EDP is interpreted as a twinned (or composite, i.e., [100]
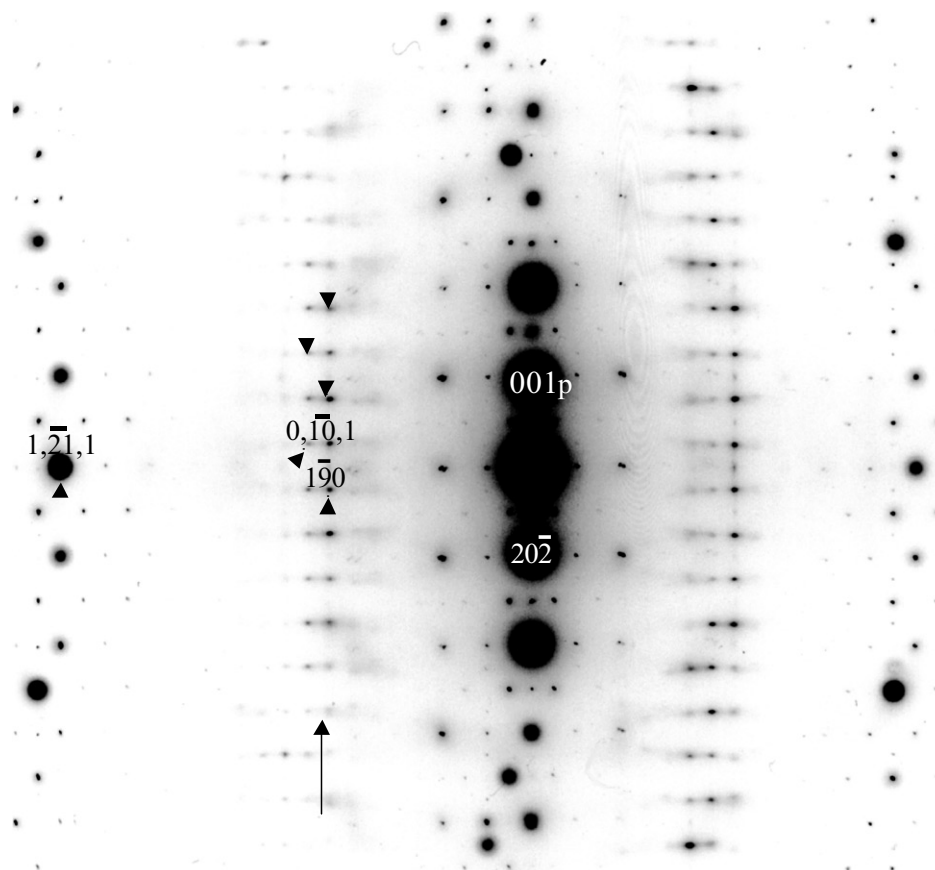
Fig. 4. Shows an EDP obtained by tilting 5–10° away from the exact $[100]_p$ zone axis orientation of Fig. 2b (keeping the $[001]_p^*$ systematic row excited) so as to bring up the various satellite HOLZ layer reflections. Note the doubled density of reflections in alternate HOLZ layers (one such HOLZ layer is arrowed in Fig. 4) and the presence of streaking (again along $[010]_p^*$) in these double density layers. The parent perovskite-type reflections are shown labelled with a subscript p. Indexation without the subscript p is with respect to an $\mathbf{a} = 2a_p - 2c_p$, $\mathbf{b} = 4b_p$, $\mathbf{c} = 2a_p + 2c_p$ ($\mathbf{a}^* = 1/4\,[10\bar{1}]_p^*$, $\mathbf{b}^* = 1/4\,[010]_p^*$, $\mathbf{c}^* = 1/4\,[101]_p^*$) supercell.

and [001] together) zone axis EDP. Removing the satellite reflections observed at the [001] zone axis orientation (see Fig. 3b) from Fig. 3a leaves reflections which obey the condition $F(0kl) = 0$ unless k is even just as would be expected for a C-centered resultant structure. A single domain [100] EDP has to date yet to be obtained due to the fine scale of the second type of twinning.

The one remaining zone axis EDP needed to assign a space group, the [010] zone axis EDP, is shown in Fig. 5. Here reflections $h\,0\,l$ are only observed if both h as well as l are even. The former condition is expected because of C-centering. The latter requires the presence of a c glide perpendicular to $\mathbf{b}$. The resultant space group is thus at least $C1c1$ but most probably $Cmcm$ ($\mathbf{a} = 2a_p - 2c_p$, $\mathbf{b} = 4b_p$, $\mathbf{c} = 2a_p + 2c_p$; $\mathbf{a}^* = 1/4\,[10\bar{1}]_p^*$, $\mathbf{b}^* = 1/4\,[010]_p^*$, $\mathbf{c}^* = 1/4\,[101]_p^*$). (We cannot, however, on the basis of the above ED evidence alone rule out the possibility of a space group intermediate between $C1c1$ and $Cmcm$.) Such a supercell has not previously been reported for an oxygen-deficient perovskite of this type and is not compatible with any

known to date supercell arising from oxygen vacancy ordering [30–32].

3.4. Group theoretical considerations

When thinking about the significance of the above fine scale twinning, it is important to recognize that there exists a strong, F-centered sub-set of sharp, well-defined Bragg reflections (see Figs. 2–5), corresponding to an intermediate 'parent' structure, associated with the above supercell (indeed only these F-centered reflections can be observed at all in XRD patterns) and that the weaker and somewhat streaked (along $[010]_p^*$) class of additional satellite reflections which lower the resultant space group symmetry from F- to C-centered arise from a condensed $\mathbf{q} = \mathbf{c}^*$ modulation of this intermediate parent structure. Given the tetragonal metric symmetry observed by XRD, it is reasonable to suggest that this intermediate parent structure must have tetragonal symmetry (with the four-fold axis running along $\mathbf{b}$) and space group symmetry of at least $F4/m$ (given the glide plane extinction condition of Fig. 5) but possibly
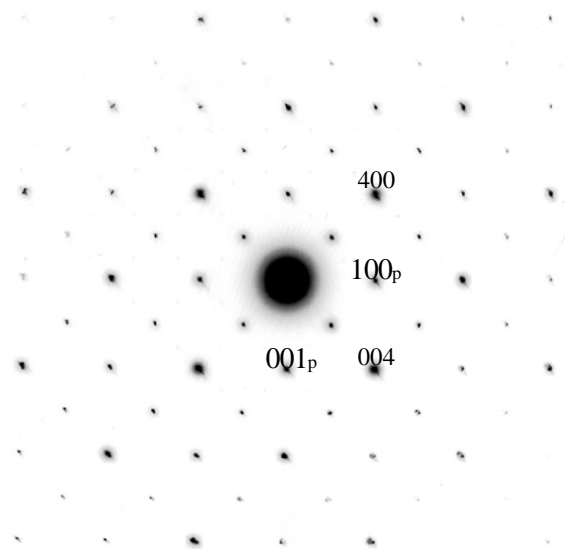
Fig. 5. A typical $[010]_p$ zone axis EDP. Here reflections $h\,0\,l$ are only observed if both h as well as l are even. The former condition is expected because of C-centering. The latter requires the presence of a c glide perpendicular to $\mathbf{b}$. The parent perovskite-type reflections are shown labelled with a subscript p. Indexation without the subscript p is with respect to an $\mathbf{a} = 2a_p - 2c_p, \mathbf{b} = 4b_p, \mathbf{c} = 2a_p + 2c_p$ ($\mathbf{a}^* = 1/4\,[10\bar{1}]_p^*, \mathbf{b}^* = 1/4\,[010]_p^*, \mathbf{c}^* = 1/4\,[101]_p^*$) supercell.

as high as $F4/mmm$. (Note that the standard setting for these latter two space groups, $I4/m$ and $I4/mmm$ respectively, would require a change in the above supercell setting to $\mathbf{a}' = 2a_p$, $\mathbf{b}' = 2b_p$, $\mathbf{c}' = 4c_p$.)

Given such a metrically tetragonal intermediate parent structure, condensed $\mathbf{q} = \mathbf{a}^* \equiv 1/4\,[10\bar{1}]_p^*$ and $\mathbf{q} = \mathbf{c}^* \equiv 1/4\,[101]_p^*$ modulations become symmetry equivalent and give rise to distinct orientational twin variants. Furthermore, given that a condensed $\mathbf{q} = \mathbf{c}^*$ modulation does not lower the metric symmetry from tetragonal to orthorhombic, alternation from one twin variant to the other and back again (across an $[010]_p$ twin plane) could be expected to often occur on a reasonably fine scale. Micro-twinning of this sort can be expected to give rise to what are in effect stacking faults characterized by shift vectors $\mathbf{R}$ corresponding to Bravais lattice vectors of the parent F-centered structure which are lost in the transition to the final resultant C-centered structure (see, e.g., Ref. [37]), i.e., to shift vectors $\mathbf{R}$ of the type $1/2\,(\mathbf{b} + \mathbf{c})$ or equivalently $1/2\,(\mathbf{c} + \mathbf{a})$. The dot product of all F-centered parent reflections with $\mathbf{R}$ is by definition zero and thus these reflections remain unaffected by the twinning while the dot product of the additional C-centered reflections with $\mathbf{R}$ is no longer zero thus explaining why only this class of reflections should be streaked and not the intermediate parent reflections [37], just as is observed experimentally.

3.5. Structural modelling and Rietveld refinement

Having established supercells and probable space group symmetries for both the resultant superstructure as well as the intermediate parent structure, the question becomes what sort of atomic ordering and associated structural relaxation is responsible? The structures of **1–3** were thus refined via the Rietveld method using synchrotron powder diffraction data.

Given the weakness and the streaked character of the non-F-centered satellite reflections in the ED data coupled with their complete absence in the XRD data, only the intermediate parent structure could be meaningfully refined. The initial structure model/s were thus based on a $2a_p \times 2a_p \times 4c_p$ supercell of a parent perovskite structure in space group $I4/mmm$ (note the transformation of the axes relative to the discussion above to give the standard crystallographic setting for this space group). There are only two possible locations for the four-fold axis given a perovskite parent structure, running through the Co ions or running through the Ln/Sr ions. It was found that the low 2θ satellite reflections primarily associated with compositional ordering ($2\theta < \sim 15°$) could only be fitted satisfactorily with the four-fold axis running through the latter Ln/Sr ions. Having established the siting of the four-fold axis with respect to the perovskite parent structure, there still remained two potential locations for the orthogonal mirror plane—running through an (001) plane of Ln/Sr ions or running mid-way between two such planes. A satisfactory refinement could only be obtained for the latter.

The initial positions of the ions within this $I4/mmm$, $2a_p \times 2a_p \times 4c_p$ supercell were then placed at those expected for an ideal undistorted perovskite parent structure. The relative site occupancies of the different ions were initially set at their nominal compositions, with the Sr^{2+} and rare earth (Ln^{3+}) ions disordered over the three distinct sites in this $I4/mmm$ supercell. The oxygen sites were initially set as fully occupied. Refinement of isotropic thermal parameters indicated sites where substantial oxygen deficiency and/or Sr^{2+}/ Ln^{3+} disorder were present. While essentially no X-ray contrast is present in **1** between isoelectric Sr^{2+} and Y^{3+} ions, this is not the case between Sr^{2+} and the Dy^{3+}/Ho^{3+} ions. Refinement of the site occupancies for samples **2** and **3** suggested that rare earth Ln^{3+} ions exclusively occupy the (Ln1) $4e$ (0,0,z: $z \sim 0.145$) sites, Sr^{2+} ions exclusively occupy the (Sr2) $4e$ (0,0,z: $z \sim 0.625$) sites, while both ions are disordered over the (Sr3/Ln3) $8g$ (0,1/2,z: $z \sim 0.134$) sites (Table 2). Similar treatment of the oxygen sites revealed that the oxygen vacancies in the structure were found to be present on the (O2) $8i$ (x,0,0 : $x \sim 0.255$) sites (Table 2). Given the strong correlations that were present between site occupation factors and isotropic thermal parameters,

Table 2
Fractional atomic coordinates and isotropic thermal parameters (B_{iso}) ($\text{Å}^2 \times 100$) for **1**, **2** and **3** with Esds in parentheses

	1	**2**	**3**
Formula	$Y_{0.33}Sr_{0.67}CoO_{2.79}$	$Dy_{0.33}Sr_{0.67}CoO_{2.78}$	$Ho_{0.33}Sr_{0.67}CoO_{2.76}$
Co1 x (8h: ($x,x,0$))	0.2493(5)	0.2486(4)	0.2495(4)
B_{iso}	0.7(1)	0.2(1)	0.3(1)
Co2 B_{iso} (8f: (1/4,1/4,1/4))	0.7(1)	0.2(1)	0.3(1)
Ln1 z (4e: (0,0,z))	0.1488(1)	0.1446(1)	0.1479(1)
B_{iso}	0.4(1)	0.8(1)	0.6(1)
Sr2 z (4e: (0,0,z))	0.6200(3)	0.6230(2)	0.6226(2)
B_{iso}	0.4(1)	0.8(1)	0.6(1)
Sr3/Ln3 z (8g: (0,1/2,z))	0.1344(2)	0.1325(2)	0.1336(1)
B_{iso}	0.4(1)	0.8(1)	0.6(1)
SOF[a] (Sr:Ln)	0.83/0.17	0.83/0.17	0.83/0.17
O1 x (16m: (x,x,z))	0.2213(12)	0.2219(10)	0.2220(11)
O1 z	0.1223(5)	0.1220(7)	0.1236(6)
B_{iso}	3.0(1)	3.2(1)	4.1(1)
O2 x (8i: ($x,0,0$))	0.2547(7)	0.2557(7)	0.2562(8)
B_{iso}	3.0(1)	3.2(1)	4.1(1)
SOF[b]	0.58	0.56	0.52
O3 x (8j: ($x,1/2,0$))	0.2265(10)	0.2284(8)	0.2224(9)
B_{iso}	3.0(1)	3.2(1)	4.1(1)
O4 y (16n:(0,y,z))	0.2461(9)	0.2468(7)	0.2469(11)
O4 z	0.2532(8)	0.2528(9)	0.2562(8)
B_{iso}	3.0(1)	3.2(1)	4.1(1)
R_P/R_{WP}	3.0%/4.1%	2.7%/3.8%	3.0%/4.1%

[a] Set as nominal composition.
[b] As determined from thermogravimetric analysis.
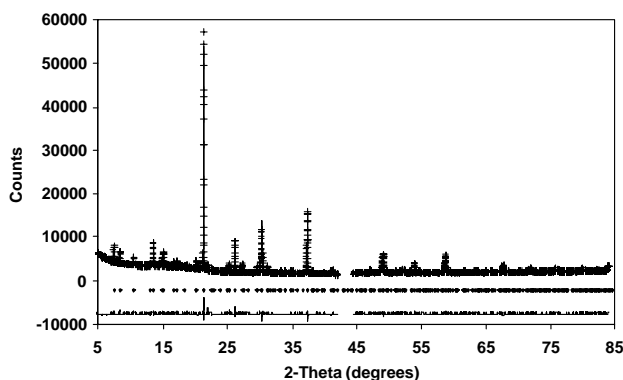
Fig. 6. The observed, calculated and difference synchrotron diffraction profiles for $Ho_{0.33}Sr_{0.67}CoO_{2.76}$ (**3**).

as well as the relatively weak scattering power of oxygen atoms in the presence of heavy metal atoms the O2 site occupation factor was set at the value determined by thermogravimetry.

The observed, calculated and difference synchrotron diffraction profiles for $Ho_{0.33}Sr_{0.67}CoO_{2.76}$ (**3**) resulting from these refinements are shown in Fig. 6 while the refined structure of **3** is displayed in Fig. 7. The crystallographic data obtained for **1**–**3** by Rietveld refinement using synchrotron powder diffraction data are given in Table 1, while the atomic coordinates and isotropic thermal parameters (B_{iso}) for **1**–**3** are given in Table 2. Note that the Sr3/Ln3 and O2 sites remain

partially occupied in these intermediate parent structures. Further Ln/Sr or O/vacancy ordering may well be responsible for the additional weak satellite reflections present in the ED data but too weak to be observed in the XRD data. It is not possible to say from the data we have available. Calculated bond lengths are given in Table 3, and selected O–Co–O bond angles in Table 4.

4. Discussion and conclusions

Compared to related $Ln_{1-x}Sr_xCoO_{3-\delta}$ perovskite phases containing larger lanthanide ions such as La and Nd, the rare earth Ln^{3+} ions in **1**–**3** are substantially (~ 17–18%) smaller than the Sr^{2+} ions [38]. It is not therefore perhaps surprising that this large size difference leads to Ln/Sr ordering in the present case. It is, for the same reason, noteworthy that the $La_{1-x}Sr_xCoO_{3-\delta}$ and $Nd_{1-x}Sr_xCoO_{3-\delta}$ systems display solid solution behavior across the entire doping range ($0 \leqslant x \leqslant 1$) while our study, by contrast, has found single-phase $Ln_{1-x}Sr_xCoO_{3-\delta}$, ($Ln = Y^{3+}$, Dy^{3+} and Ho^{3+}) perovskite samples of the current type were only able to be prepared for $0.60 \leqslant x \leqslant 0.9$. (This limited extent of the solid solution range when the Ln/Sr size difference becomes too large is in dispute with extended solid solution ranges ($0 \leqslant x \leqslant 1$) that have previously been reported by Yo and co-workers for smaller rare earth ions such as Sm [22], Gd [23] and Dy [24]. Examination of their published diffraction

profiles for $Dy_{1-x}Sr_xCoO_{3-\delta}$, in Ref. [24] reveals that their samples for $0 < x \leqslant 0.50$ appear to be comprised of two or more phases.)

Whilst a neutron diffraction study may ultimately prove to be necessary to give the clearest picture of the nature of the local oxygen coordination around the $Ln1$ and $Sr3/Ln3$ sites, the results of this study suggest that
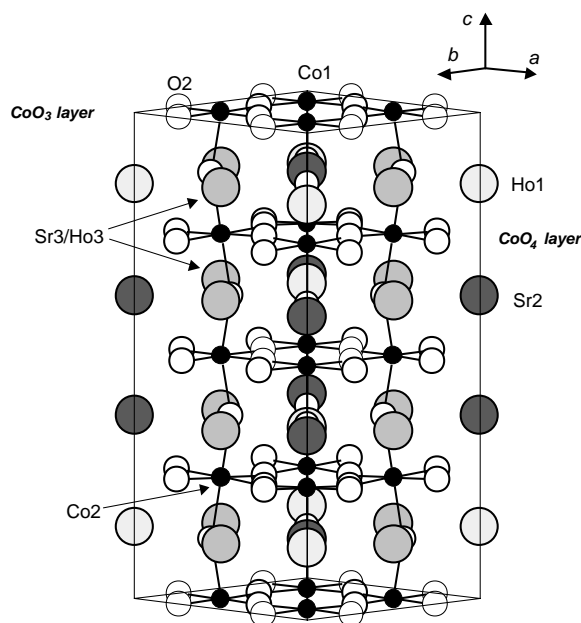

Fig. 7. The refined structure of $Ho_{0.33}Sr_{0.67}CoO_{2.76}$ (3) in a projection close to a supercell $\langle 110 \rangle$ direction. Note the CoO_3 layers at $z = 0$ and 1/2 and the CoO_4 layers at $z = 1/4, 3/4$. Approximately 50% of the O2 sites (indicated by a thin-rimmed white atom) are vacant. Each of the rare earth layers contains one $Ln1$ ion, one Sr2 ion and two disordered (Sr3/Ho3) sites, giving a Sr:Ho ratio of 3:1.

the oxygen vacancies within these structures primarily reside on O2 sites. Fig. 7 shows that these vacant O2 sites exist in the basal planes at $z = 0$ and 1/2, leading to an approximate layer composition of CoO_3. The cobalt containing layers at $z = 1/4$ and 3/4 on the other hand have compositions of CoO_4. The relative impact of this oxygen vacancy ordering pattern (along the c-axis with a $z = 1/2$ repeat) may be observed by comparing Fig. 1a with b and c at low angle. Given that essentially no contrast is present due to Y^{3+} and Sr^{2+} ions, the supercell reflections at low angle in Fig. 1a are mainly due to oxygen vacancy ordering. The additional low angle ($2\theta < 15°$) supercell reflections for 2 and 3 arise from Ln/Sr cation ordering on the $Ln1$, Sr2 and Sr2/$Ln3$ ($Ln = Dy$ or Ho) sites. Although the distribution of vacant O2 sites within the xy plane in not clear from this study, there is the suggestion that the average oxygen coordination about the $Ln1$ rare earth site is 10-fold rather than the typical 12-fold A-site perovskite coordination.

In only a few instances has it been reported that perovskite-based oxides containing Sr^{2+} and small rare earth ions such as Y^{3+}, Dy^{3+} and Ho^{3+} form structures with both ionic species disordered over the same crystallographic site [39–44]. The substantial difference in ionic radii between Sr^{2+} and Ln^{3+} (Y^{3+}, Dy^{3+} and Ho^{3+}) typically leads to ordering over different sites within the crystal lattice. The structures formed by 1–3 are similar to those reported in Ref. [43], where both fully ordered (Sr^{2+}) and disordered (Sr^{2+}/Ln^{3+}) sites are present. Examination of the average "A site"–O bond lengths in the $Ln_{0.33}Sr_{0.67}CoO_{3-\delta}$, phases clearly reflect the ordering of the Sr^{2+} and Ln^{3+} ions. The average oxygen bond lengths to the fully ordered rare

Table 3
Selected bond lengths (Å) for **1**, **2** and **3** with Esds in parentheses

	1	**2**	**3**
Bond	$Y_{0.33}Sr_{0.67}CoO_{2.79}$	$Dy_{0.33}Sr_{0.67}CoO_{2.78}$	$Ho_{0.33}Sr_{0.67}CoO_{2.76}$
Co1–O1 ($\times 2$)	1.899(8)	1.894(6)	1.916(7)
Co1–O2 ($\times 2$)[a]	1.902(4)	1.894(3)	1.902(4)
Co1–O3 ($\times 2$)	1.920(7)	1.920(5)	1.919(6)
Co2–O1 ($\times 2$)	1.982(8)	1.987(7)	1.958(7)
Co2–O4 ($\times 4$)	1.908(6)	1.904(7)	1.907(8)
$Ln1$–O1 ($\times 4$)	2.422(6)	2.414(5)	2.421(5)
$Ln1$–O2 ($\times 4$)[b]	2.997(7)	2.951(6)	2.989(6)
$Ln1$–O3 ($\times 4$)	2.467(7)	2.507(7)	2.507(9)
Sr2–O1 ($\times 4$)	3.007(11)	2.994(9)	2.995(9)
Sr2–O3 ($\times 4$)	2.782(9)	2.799(8)	2.828(9)
Sr2–O4 ($\times 4$)	2.702(9)	2.677(9)	2.642(11)
Sr3/$Ln3$–O1 ($\times 4$)	2.721(10)	2.713(9)	2.715(9)
Sr3/$Ln3$–O2 ($\times 2$)[c]	2.784(8)	2.755(7)	2.763(6)
Sr3/$Ln3$–O3 ($\times 2$)	2.690(9)	2.675(8)	2.655(7)
Sr3/$Ln3$–O4 ($\times 2$)	2.658(10)	2.669(9)	2.691(9)
Sr3/$Ln3$–O4 ($\times 2$)	2.592(9)	2.610(10)	2.563(9)

[a] Expected number of Co1–O2 bonds for **1**: 1.16, **2**: 1.12, **3**: 1.04.
[b] Expected number of $Ln1$–O2 bonds for **1**: 2.32, **2**: 2.24, **3**: 2.08.
[c] Expected number of Sr3/$Ln3$–O2 bonds for **1**: 1.16, **2**: 1.12, **3**: 1.04.

Table 4
Selected bond angles (deg) for **1**, **2** and **3** with Esds in parentheses

	1	**2**	**3**
Bond angle	$Y_{0.33}Sr_{0.67}CoO_{2.79}$	$Dy_{0.33}Sr_{0.67}CoO_{2.78}$	$Ho_{0.33}Sr_{0.67}CoO_{2.76}$
O1–Co1–O1	161.7	162.5	162.2
O1–Co1–O2	83.7	84.0	83.9
O1–Co1–O3	95.8	95.7	95.6
O2–Co1–O2	92.5	93.3	93.0
O2–Co1–O3	176.0	177.0	175.3
O2–Co1– O3	83.6	83.8	82.3
O3–Co1–O3	100.4	99.2	102.34
O1–Co2–O1	180	180	180
O1–Co2–O4	85.0	85.0	86.5
O1–Co2–O4	95.0	95.0	93.5
O4–Co2–O4	180	180	180
O4–Co2–O4	88.2	88.5	88.4
O4–Co2–O4	91.8	91.5	91.6

earth ($Ln1$) sites in **1–3** range between 2.568(6) and 2.572(7) Å; the fully ordered strontium (Sr2) sites range between 2.822(10) and 2.830(10) Å and the disordered mixed (Sr3/$Ln3$) sites range between 2.677(8) and 2.688(9) Å. These values are consistent with 12-fold coordinate Sr–O bond lengths of 2.84 Å and 10-fold Ln–O bond lengths of 2.52 Å observed in other compounds [38]. Further Ln/Sr and/or O/vacancy ordering may be causing the additional weak satellite reflections present in the ED data but too weak to be observed in the XRD data.

The results of the structure refinements provide little indication of ordering between Co^{3+} and Co^{4+} within **1–3**. It might be expected that Co^{4+}–O bonds should be substantially shorter ($\sim$1.93 Å) than Co^{3+}–O bonds ($\sim$2.01 Å) [38], however both the Co1 and Co2 sites show Co–O bond lengths $<$1.92 Å. On average, the Co2–O bonds appear to be longer than the Co1–O bonds although this may be more a reflection of the anisotropic Co2–O$_6$ coordination sphere.

Bond valence sum calculations (see, for example, Ref. [45]) likewise give no clear indication for Co^{3+}/Co^{4+} ordering, e.g., for $Ho_{0.33}Sr_{0.67}CoO_{2.76}$, Co1 is nominally bonded to two O1's at a distance of 1.916 Å (AV, see Ref. [45], of 0.561), two nominally 0.52 occupied O2's at 1.902 Å (AV = 0.582) and to two O3's at 1.919 Å (AV = 0.554). The possible AV of Co1 thus ranges from 2.229 if both local O2 sites are vacant (presumably such a local four-fold coordination is thus the most unlikely local configuration), 2.811 if one is occupied and the other vacant (quite possible) or 3.392 if both local O2 sites are occupied (also quite possible). These conclusions however assume that there is no local relaxation away from the refined average position dependent upon the local oxygen ion coordination. Co2, on the other hand, is bonded to two O1's at 1.958 Å (AV, see Ref. [45], of 0.499) and four O4's at 1.907 Å (AV of 0.573). The bond valence sum, or AV, of Co2 is thus 3.289. The

R_0 parameter for Co^{3+}–O^{2-} (see Ref. [45]) has been used for these bond valence sum calculations as [45] list no equivalent R_0 parameter for Co^{4+}–O^{2-}. Very similar numbers occur for both the Ln = Y and Dy compounds.

In conclusion, coupled Ln/Sr and O/vacancy ordering and associated structural relaxation have been shown to be responsible for the existence of a complex, previously unreported, perovskite-related superstructure phase in the $Ln_{0.33}Sr_{0.67}O_{3-\delta}$ (Ln = Y, Ho and Dy) systems.

Acknowledgments

References

[1] S.J. Skinner, Int. J. Inorg. Mater. 3 (2001) 113.

[2] H.Y. Tu, Y. Takeda, N. Imanishi, O. Yamamoto, Solid State Ionics 100 (1997) 283.

[3] R.H.E. van Doorn, A.J. Burggraaf, Solid State Ionics 128 (2000) 65.

[4] S.B. Adler, Solid State Ionics 111 (1998) 111.

[5] A.V. Kovalevsky, V.V. Kharton, V.N. Tikhonovich, E.N. Naumovich, A.A. Tonoyan, O.P. Reut, L.S. Boginsky, Mater. Sci. Eng. B 52 (1998) 105.

[6] V.V. Kharton, A.A. Yaremchenko, A.V. Kovalevsky, A.P. Viskup, E.N. Naumovich, P.F. Kerko, J. Membrane Sci. 163 (1999) 307.

[7] S. Mukherjee, R. Ranganathan, P.S. Anikumar, P.A. Joy, Phys. Rev. B 54 (1996) 9367.

[8] P.S. Anil Kumar, P.A. Joy, S.K. Date, J. Phys.: Condens. Matter 10 (1998) L487.

[9] D.N.H. Nam, K. Jonason, P. Nordblad, N.V. Khiem, N.X. Phuc, Phys. Rev. B 59 (1998) 4189.

[10] K. Asai, O. Yokokura, N. Nishimori, H. Chou, J.M. Tranquada, G. Shirane, S. Higuchi, Y. Okajima, K. Kohn, Phys. Rev. B 50 (1994) 3025.

[11] M.A. Senaris-Rodriguez, J.B. Goodenough, J. Solid State Chem. 118 (1995) 323.

[12] R. Caciuffo, D. Rinaldi, G. Barucca, J. Mira, J. Rivas, M.A. Senaris-Rodriguez, P.G. Radaelli, D. Fiorani, J.B. Goodenough, Phys. Rev. B 59 (1999) 1068.

[13] J. Mira, J. Rivas, M. Vazquez, J.M. Garcia-Beneytez, J. Arcas, R.D. Sanchez, M.A. Senaris-Rodriguez, Phys. Rev. B 59 (1999) 123.

[14] R. Ganguly, I.K. Gopalakrishnan, J.V. Yakhmi, Physica B 271 (1999) 116.

[15] S. Chaudhary, S.B. Roy, P. Chaddah, J. Alloys Compds. 326 (2001) 112.

[16] G.H. Jonker, J.H. Van Santen, Physica 19 (1953) 120.

[17] J.B. Goodenough, J. Phys. Chem. Solids 6 (1958) 287.

[18] P.M. Raccah, J.B. Goodenough, J. Appl. Phys. 39 (1968) 1209.

[19] G. Thornton, B.C. Tofield, A.W. Hewat, J. Solid State Chem. 61 (1986) 301.

[20] J. Mizusaki, J. Tabuchi, T. Matsuura, S. Yamauchi, K. Fueki, J. Electrochem. Soc. 136 (1989) 2082.

[21] M.A. Senaris-Rodriguez, M.P. Breijo, S. Castro, C. Rey, M. Sanchez, R.D. Sanchez, J. Mira, A. Fondado, J. Rivas, Int. J. Inorg. Mater. 1 (1999) 281.

[22] K.H. Ryu, K.S. Roh, S.J. Lee, C.H. Yo, J. Solid State Chem. 105 (1993) 550.

[23] J.W. Kang, K.H. Ryu, C.H. Yo, Bull. Korean Chem. Soc. 17 (1995) 600.

[24] S.K. Jeong, M.G. Kim, K.H. Kim, C.H. Yo, Bull. Korean Chem. Soc. 17 (1996) 794.

[25] P.V. Vanitha, A. Arulraj, P.N. Santhosh, C.N.R. Rao, Chem. Mater. 12 (2000) 1666.

[26] K. Yoshii, H. Abe, A. Nakamura, Mater. Res. Bull. 36 (2001) 1477.

[27] P. Berastagui, S. Hull, F.J. García-García, S.-G. Eriksson, J. Solid State Chem. 164 (2002) 119.

[28] M. Mitome, M. Okamoto, Y. Bando, H. Yamamura, J. Vac. Sci. Technol. B 19 (2001) 2284.

[29] C.J. Howard, R.L. Withers, B.J. Kennedy, J. Solid State Chem. 160 (2001) 8.

[30] P. Hagenmuller, M. Pouchard, J.-C. Grenier, Solid State Ionics 43 (1990) 7.

[31] M.T. Anderson, J.T. Vaughey, K.R. Poeppelmeier, Chem. Mater. 5 (1993) 151.

[32] A.I. Becerro, C. McCammon, F. Langenhorst, F. Seifert, R. Angel, Phase Transitions 69 (1999) 133.

[33] M. Karpinnen, M. Matvejeff, K. Salomaeki, H. Yamauchi, J. Mater. Chem. 12 (2002) 1761.

[34] Z. Barnea, D.C. Creagh, T.J. Davis, R.F. Garrett, S. Jansky, A.W. Stevenson, S.W. Wilkins, Rev. Sci. Instrum. 63 (1992) 1069.

[35] H.M. Rietveld, J. Appl. Crystallogr. 2 (1969) 65.

[36] B.A. Hunter, Rietica—A Visual Rietveld Program, Vol. 20, Commission on Powder Diffraction Newsletter, 1998, p. 21; available at: http://www.iucr.org/iucr-top/comm/cpd/Newsletters/

[37] L. Norén, G. Van Tendeloo, R.L. Withers, J. Solid State Chem. 162 (2001) 122.

[38] R.D. Shannon, Acta Crystallogr. A 32 (1976) 751.

[39] M. James, J.P. Attfield, J. Solid State Chem. 105 (1993) 287.

[40] M. James, J.P. Attfield, Physica C 235–240 (1994) 751.

[41] M. James, J.P. Attfield, Chem. Commun. 10 (1994) 1185.

[42] M. James, J.P. Attfield, J. Rodriguez-Carvajal, Chem. Mater. 7 (1995) 1448.

[43] P.D. Battle, J.E. Milburn, M.J. Rosseinsky, L.E. Spring, J.F. Vente, Chem. Mater. 9 (1997) 3136–3143.

[44] I.B. Sharma, D. Singh, S.K. Magotra, J. Alloys Compds. 269 (1998) 13.

[45] N.E. Brese, M. O'Keeffe, Acta Crystallogr. B 47 (1991) 192.